J. Appl. Comput. Mech., xx(x) (2026) 1-14
DOI: 10.22055/jacm.2026.49138.5760

ISSN: 2383-4536
jacm.scu.ac.ir

Shahid Chamran University of Ahvaz

Journal of Applied and Computational Mechanics

Research Paper

Statistical, Numerical, and Experimental Analysis of Thickness-Graded Adhesive for Enhancing Single-Lap Joint Strength

S.M.M.M.H. Ahari, J. Eskandari Jam, M.H. Alaei, H. Momeni, P. Pirali

Faculty of Materials and Manufacturing Technologies, Malek Ashtar University of Technology, Tehran, Iran,
Email: Mahyar.ahari90@gmail.com (S.M.M.M.H.A.); eskandari@mut.ac.ir (J.E.J.); mhallaee@mut.ac.ir (M.H.A.); h_momeni@mut.ac.ir (H.M.); ppirali@mut.ac.ir (P.P.)

Received February 06 2026; Revised June 18 2026; Accepted for publication July 07 2026.
✉ Corresponding author: J. Eskandari Jam (eskandari@mut.ac.ir)

Abstract. This research examined the adhesive joint strength between aluminum (Al) and glass-epoxy composite (GL) adherents using graded adhesive through the thickness of the joint (thickness-graded adhesive). Single-lap joints with thickness-graded adhesive were fabricated and subjected to tensile loading. Tensile strength was predicted with finite element simulations employing cohesive zone and shear-damage modeling, and compared with experimental outcomes. Statistical analysis and optimization were performed utilizing response surface methodology (RSM), incorporating total adhesive thickness, adhesive layer thickness ratio, and adherend type as variables. Findings revealed a significant correlation between the shear damage model and experimental results, with adhesive grading enhancing joint strength by 48%. Optimization via RSM indicated that peak tensile force was attained with a total adhesive thickness of 1mm, adhesive layer thickness ratio of 0.85, and GL-GL adherent type.

Keywords: Single-lap joint; Thickness-graded adhesive; Shear damage; CZM; RSM.

1. Introduction

Adhesive bonding has gained widespread adoption in the automotive, aerospace, and civil engineering sectors for structural assembly and reinforcement, primarily due to its advantages in weight reduction, corrosion resistance, and minimal adherend-related damage [1, 2]. A primary challenge in adhesive joints is the occurrence of stress concentrations at the extremities of the overlap, arising from material property discontinuities and sharp geometric transitions near the bondline [3].

These localized stresses can substantially compromise joint integrity and induce premature failure. To counteract this, various mitigation strategies have been developed, including adhesive spew fillets at overlap edges and adherend geometry optimization [4]. An innovative solution lies in functionally graded adhesives (FGA), engineered with composition gradients tailored to in-service loading [5, 6]. Research confirms that FGA outperforms geometric modifications in attenuating edge stress peaks and achieving homogeneous stress fields within the joint [7-9]. Stiff, brittle adhesives at overlap ends exacerbate stress concentrations. Hybrid adhesive systems combine rigid and compliant adhesives to optimize load transfer while suppressing stress singularities. In FGA joints, ductile adhesives are strategically placed at the overlap termini to dampen stress peaks, and stiffer adhesives are positioned centrally to enhance load-carrying capacity and limit plastic deformation, thereby elevating overall joint strength [7].

Volkersen's theory posits that softer adhesives at these locations reduce peak stresses and promote uniform stress distribution [10]. Daiden et al. [11] conducted combined experimental and numerical analyses on the lap-shear performance of graded adhesive joints comprising glass-epoxy composite and 7075 aluminum adherends [11]. Symmetric adhesive grading increased the baseline configuration-related failure load by 206%. Kim et al. [12] evaluated failure loads in single-lap joints with spatially varying adhesive properties, employing Taguchi and response surface methodologies. Optimal performance was achieved with extended overlap, reduced bondline thickness, lower ductile adhesive fraction, and steel–steel adherends. Berto et al. [13] performed finite element simulations on hybrid single-lap joints with glass-epoxy composite and aluminum adherents, implementing continuous adhesive property gradients along the overlap. Results showed a 70% improvement in strength over monolithic adhesive systems. Jia et al. [14] integrated graphene nanoplatelets (GNP) into epoxy resin to produce high-modulus composite adhesives (centrally located within the bondline) and medium-modulus neat epoxy at the edges, establishing a modulus gradient. The optimized FGA configuration exhibited 210.1% higher failure load and 350% greater elongation at break. Beyond longitudinal stress distribution, transverse stress variation through the adhesive thickness plays a pivotal role in joint performance. The effect of bondline thickness on single-lap joint strength is known, with most studies about structural adhesives reporting a reduction in strength with increasing thickness. Adams et al. [15] noted that greater adhesive thickness heightens the risk of internal flaws (e.g., voids, microcracks), accelerating failure. Crocombe [16] showed that thicker joints experience strength degradation due to adhesive plasticity. Gleich et al. [17] used finite element analysis to demonstrate that the increase in bondline thickness leads to higher peel and shear stress, thereby reducing the joint's failure load [17]. In automotive epoxy-bonded joints, Grant et al. [18] similarly observed that strength

Published online: September 18 2026

decreases with increasing thickness. Ciardiello et al. [19] applied polyurethane adhesive across adherent types (CS-CS and MS-CS versus MS-MS), reporting 45% and 30% reductions in shear strength. Wang et al. [20] explored adhesive properties and the effects of thickness on CFRP- steel single-lap joints [20].

For ductile adhesives, increasing thickness from 0.5 mm to 1.5 mm improved fracture energy but decreased interfacial stiffness. Nasr Saleh et al. [21] studied mode I fractures in thick marine adhesive joints, finding that ductile adhesives required 4-10 times more energy for crack growth compared to their brittle counterparts [21]. Metehri et al. [22] applied Abaqus to optimize adhesive and adherend edge geometries. Rangaswamy et al. used Taguchi and neural networks to show that overlap length dominates joint strength over adhesive thickness, with minimal interactions [23]. Morgado et al. [24] inserted three adhesive interlayers between carbon plies, increasing strength by 20%. Santos et al. [25] significantly strengthened CFRP joints using titanium piles and additional interfacial adhesives, thereby markedly increasing the failure load. Multiple numerical strategies exist for modeling adhesive response, each predicting unique accuracy in strength and failure modes. Sugiman et al. [26] contrasted CZM and CDM in static failure prediction of single-lap joints. Özer et al. [27] applied the exponential Drucker-Prager (EDP) criterion to forecast failure loads in mono- and bi-adhesive joints, analyzing stress distributions at mid-thickness. Kumar et al. [28] performed 2D/3D finite element analyses using von Mises criteria to estimate failure loads. Rocha et al. [29] evaluated traction-separation laws in CZM, validating damage initiation and propagation against experiments. Portillo et al. [30] focused on the mechanical characterization of hyperelastic adhesives. They found that the Mooney-Rivlin model provided the best fit and is therefore the most suitable for modeling the behavior of such adhesives. Shishesaz et al. [31] investigated the effects of adhesive defects, adherend type, and material on stress distribution in laminated composite tubular joints subjected to axial tensile loads. They developed finite element models and solved them to validate their semi-analytical solutions. Zongkai He et al. [32] experimentally and numerically investigated the fatigue damage tolerance of CFRP/Al adhesively bonded joints and the influence of elevated temperature on fatigue performance and failure mechanisms. In their fatigue simulations, they employed the CZM to characterize the adhesive behavior. Yang et al. [33] conducted experimental and numerical investigations into the strength and failure mechanisms of single-lap adhesively bonded joints using both brittle and ductile adhesives, with CFRP and aluminum substrates, under three-point bending, low-velocity impact, and uniaxial tensile loading. To simulate the failure modes, they employed a three-dimensional CZM in the software ABAQUS. Kujawa et al. [34] conducted a comprehensive analytical, finite element, and experimental study on single-lap adhesive joints bonded with a conventional uniform epoxy adhesive. Their work provided detailed insights into stress distribution, load-carrying capacity, and analytical validation against numerical and experimental results for standard single-lap configurations. Despite extensive research on functionally graded adhesives along the overlap length to reduce stress concentrations at overlap edges, the concept of graded adhesives through the thickness of the bondline (thickness-graded adhesive) remains largely unexplored.

The main novelty of this study lies in stacking multiple adhesive layers with different thicknesses and mechanical properties in the through-thickness direction (perpendicular to the adherend surfaces) within the overlap region. This configuration creates a controlled stiffness gradient through the adhesive thickness, rather than along the overlap length. Increasing bondline thickness elevates interfacial stresses, so adhesive grading across thickness could be a promising strategy to enhance joint performance. The purpose of this study is to investigate the effects of varying adhesive properties through the bondline thickness in single-lap joints. Ductile adhesive layers were strategically placed at the adherend–adhesive interfaces, with a brittle adhesive layer positioned at the mid-plane. Numerical simulations were performed using cohesive zone modeling (CZM) and shear damage modeling, and the results were validated against experimental data. Furthermore, response surface methodology (RSM) was employed to statistically analyze the influence of key parameters, including total adhesive thickness, layer thickness ratio, and adherend type. Finally, the optimized joint configuration was fabricated and experimentally validated.

2. Materials and Methods

2.1. Materials

In this investigation, two configurations of single-lap joints were examined. The primary objective of the first configuration was to evaluate two distinct finite-element simulation approaches (the cohesive zone model and the shear damage model). The first configuration, which corresponds to the baseline article [29], employed high-strength, ductile aluminum alloy AA6082-T651 as the adherent material, AV138 brittle epoxy, 2015 ductile Araldite, and 7752 polyurethane SikaForce as the adhesive materials. The second configuration pertains to shear damage modeling of the graded adhesive joint with glass-epoxy composite (GL) and aluminum alloy AA6061-T651 (AL) as adherends, and AV138 and SikaForce 7720 as adhesives.

The joint configuration illustrated in Fig. 1 shows the mono-adhesive joint (Fig. 1(a)) and the graded adhesive region (Fig. 1(b)). In the second configuration, the adhesive bondline thickness was set to 1.5 mm, the adherends thickness to 3 mm, the adherends length to 100 mm, and the overlap length to 25 mm. The material properties employed in this study are presented in Table 1 and Table 2.

2.2. Preparation and fabrication of adhesive joint

The two-component epoxy adhesive AV138 and the two-component polyurethane adhesive SikaForce 7720 were employed to fabricate the graded adhesive joint. Aluminum AL-6061 and glass-epoxy composite were used as adherents, each with a thickness of 3 mm. The total adhesive thickness was set at 1.5 mm. To fabricate single-lap bonded joints while maintaining consistent adhesive thickness and ensuring accurate alignment of the adherends, a specialized bonding fixture was employed (Fig. 2(a)). The fixture incorporates adjustable end stops to produce joints with varying overlap lengths.

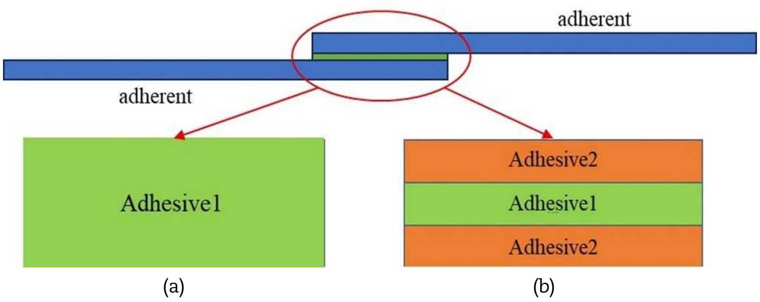

Fig. 1. Configuration of single-lap joint: (a) Mono adhesive, (b) Graded adhesive.

Table 1. Properties of adhesives [29, 35].

Properties of the adhesives	AV138	Araldite2015	Sikaforce 7752	Sikaforce 7720
Young's modulus, E (GPa)	4.89	1.85	0.49	0.1
Poisson's Ratio	0.35	0.33	0.3	0.3
Tensile yield stress, σ_y (MPa)	36.49	12.63	3.24	5
Tensile strength, σ_f (MPa)	39.45	21.63	11.48	15
Tensile failure strain, ε_f (%)	1.21	4.77	19.18	33
Shear strength, τ_y (MPa)	25.1	14.6	5.16	5
Shear strength, τ_f (MPa)	30.2	17.9	10.17	10
Shear failure strain, γ_f (%)	7.8	43.9	54.82	55
Toughness in tension, G_{IC} (N/mm)	0.2	0.43	2.36	3.24
Toughness in shear, G_{IIC} (N/mm)	0.38	4.7	5.41	6.5

Table 2. Properties of adherents [36, 37].

Properties of adherents	AL-6082-T651	AL-6061-T651
Young's modulus (GPa)	70	70
Yield Strength (MPa)	261	276
Ultimate Tensile Strength (MPa)	324	310
Elongation at Break (%)	21	17
Properties of adherent	Glass-epoxy composite (GL)	
Young's modulus, $E_{11} = E_{22}$(GPa)	25	
Shear modulus in plane, G_{12} (GPa)	4	
Shear modulus out of plane, G_{23} (GPa)	3.2	
Poisson's Ratio, ν_{12}	0.2	
Tensile strength, $X_T = Y_T$ (MPa)	380	
Compression strength, $X_C = Y_C$ (MPa)	370	
Shear strength, (MPa)	40	

Single-lap joints were first fabricated using Araldite AV138 epoxy adhesive. The adhesive was applied directly onto the aluminum adherend (Fig. 2(b)), followed by placement of the composite adherend onto the adhesive layer (Fig. 2(c)). With thickness-control implements, the bond-line thickness is precisely 1.5 mm. The fabricated single-lap joint is shown in Fig. 2(d).

The fabrication procedure for single-lap joints incorporating two different adhesives arranged in the through-thickness direction is described as follows: Since SikaForce®-7720 must be positioned at the outer layers of the bond line while allowing precise control of the desired thickness, the aluminum and composite adherends are first placed separately on the base of the fixture. An appropriate quantity of SikaForce-7720 is then applied directly to each adherend surface (Fig. 3(a)).

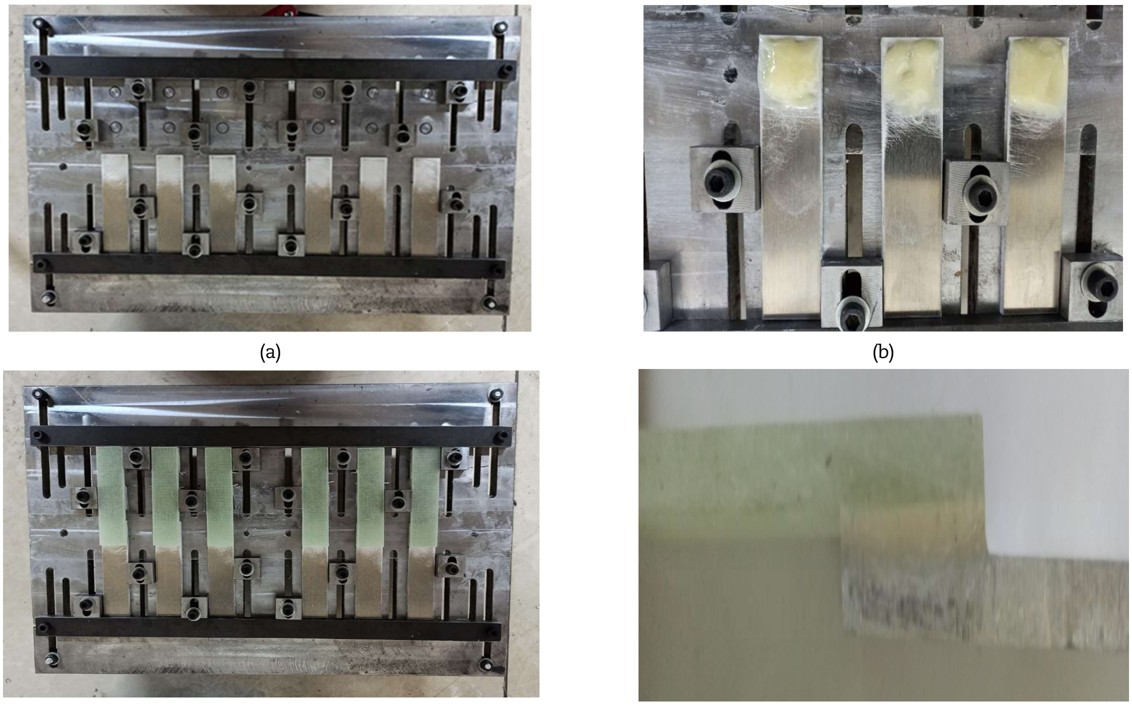

(a) (b) (c) (d)

Fig. 2. (a) Fixture of joints; (b) Applied adhesive onto the aluminum; (c) Positioning of the composite onto the aluminum; (d) Single-lap joint with a mono adhesive.

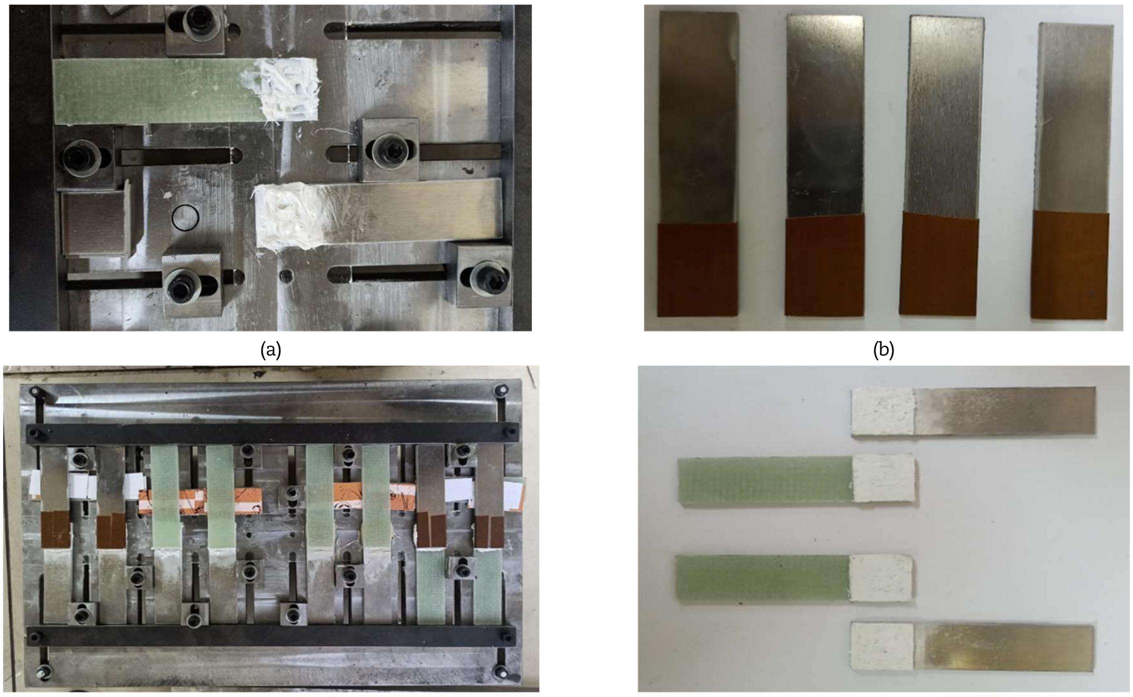

(a) (b) (c) (d)

Fig. 3. (a) Applying SikaForce-7720 onto the adherend; (b) Releasing the film around the adherend; (c) Pressing; (d) Trimming the excess adhesive.

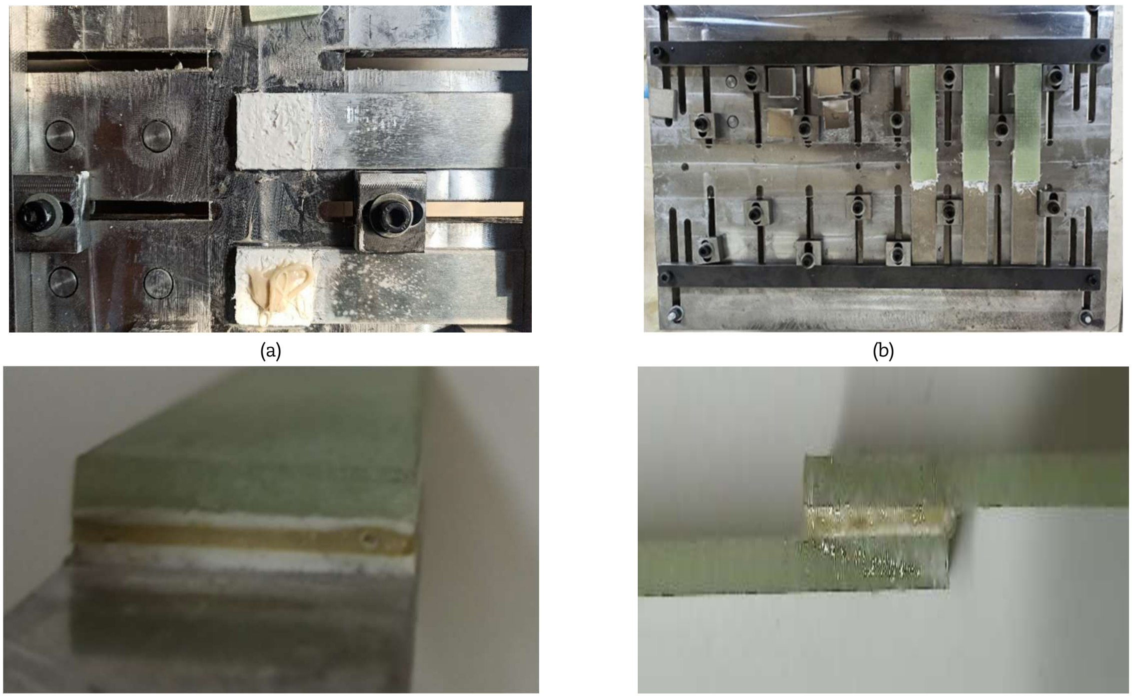

(a) (b) (c) (d)

Fig. 4. (a) Applying AV138 adhesive; (b) Placing the composite adherend onto the aluminum adherend; (c) Graded adhesive; (d) Optimized graded adhesive.

To achieve a 0.5 mm adhesive thickness on both adherends and to allow initial curing, the applied SikaForce-7720 layers are compressed using thickness-control spacer sheets. For pressing, an additional aluminum adherend was used. To prevent it from bonding to the SikaForce®-7720 adhesive in the overlap region, a release film was employed (Fig. 3(b, c)). After sufficient time to achieve the initial curing, the press assembly is removed.

Excess SikaForce-7720 that has flowed to the edges of the aluminum and composite adherends is subsequently removed by careful cleaning (Fig. 3(d)). Next, the second adhesive Araldite® AV138 is applied onto the pre-cured SikaForce-7720 layers (Fig. 4(a)). In the final assembly step, the composite adherend is placed onto the AV138 layer (Fig. 4(b)). The joint is then allowed to cure for one week at room temperature. This process yields an integrated single-lap joint featuring two distinct adhesives arranged in series along the through-thickness direction within the overlap region (Fig. 4(c)). This sequential application and staged curing approach ensure controlled layer thickness, prevents unwanted mixing of the two adhesives during assembly, and facilitates the creation of a graded adhesive bond-line with tailored through-thickness properties. Figure 4d presents the optimized graded adhesive joint design obtained from the Design of Experiments (DOE) and optimization process. The joint specimens were tested using a SANTAM testing machine in accordance with the ASTM D5868 standard [35], employing a crosshead speed of 1 nm/min (Fig. 5(a, b)).

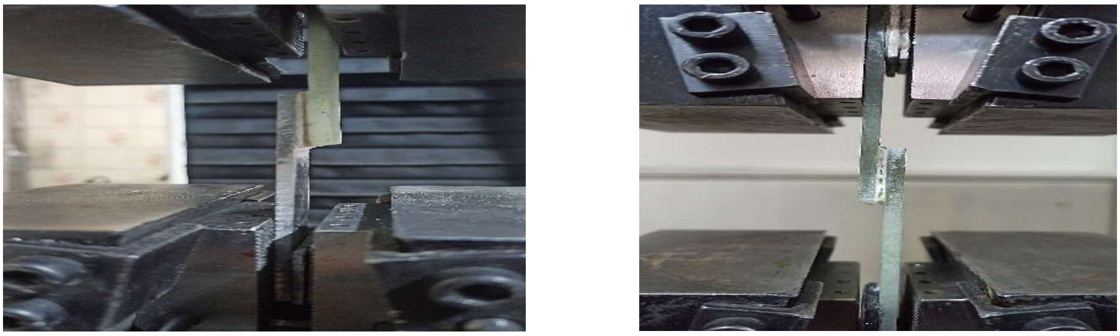

(a) (b)

Fig. 5. (a) Graded adhesive joint specimens with aluminum and composite adherend; (b) Graded adhesive joint specimens with composite and composite adherend.

2.2. Numerical modelling

In the present study, the simulations were performed using Abaqus 2021 software. In this study, two simulation approaches were employed to model the adhesive in the joint. The first approach used the cohesive zone model (CZM), and the simulation results were compared and validated against those reported in the baseline article [29]. Subsequently, the same mono adhesive joint was modeled using the shear damage model, and its results were compared with those obtained from the cohesive zone model. For graded-adhesive modeling, several elements must be assigned along the adhesive thickness for each adhesive layer. A limitation of the cohesive zone model and cohesive elements is that only a single element can be placed in the thickness direction. Consequently, the shear damage model was adopted for the simulation.

2.2.1. Cohesive Zone Model

The cohesive zone model (CZM) has been extensively employed for failure analysis in adhesive joints, metallic materials, composites, and ceramics. The CZM simulates damage mechanics based on fracture mechanics principles. The fundamental concept of the CZM is to introduce a softening traction-separation law in the damaged region surrounding the crack tip. Elements adhering to this approach are termed cohesive elements. These elements follow a traction-separation law. A key benefit is its ability to initiate and propagate damage within a unified framework, eliminating the need for predefining an initial crack.

In the CZM, the area under the traction-separation curve in tension and shear corresponds to the critical fracture toughness in mode I (G_I) and mode II (G_{II}), respectively. For the triangular traction-separation law, the adhesive behavior is assumed to be linear-elastic, both before damage initiation and after damage onset. In cohesive zone theory, damage initiation is governed by either stress-based or strain-based criteria. In the present study and for simulation validation in accordance with the baseline article [29], the quadratic nominal stress criterion was employed for damage initiation (defined by Eq. (1)), and the power-law criterion was utilized for damage propagation in the adhesive modeling (defined by Eq. (2)):

$$\left\{\frac{\langle t_n\rangle}{t_n{}^0}\right\}^2 + \left\{\frac{t_s}{t_s{}^0}\right\}^2 = 1 \tag{1}$$

$$\left\{\frac{G_I}{G_{IC}}\right\}^\alpha + \left\{\frac{G_{II}}{G_{IIC}}\right\}^\alpha = 1 \tag{2}$$

In the mixed-mode condition, the damage variable is defined within the cohesive zone model framework as the ratio of degraded stiffness to initial stiffness. The implementation of the stiffness degradation parameter in the stress components is expressed by Eq. (3):

$$\sigma = (1 - D)\bar{\sigma} \tag{3}$$

where σ denotes the current stress and $\bar{\sigma}$ represents the stress in the undamaged state. The damage variable is defined according to Eq. (4):

$$D = \frac{\delta_m^f(\delta_m - \delta_m^0)}{\delta_m(\delta_m^f - \delta_m^0)} \tag{4}$$

where δ_m represents the current displacement under mixed-mode loading, δ_m^0 denotes the displacement corresponding to the stress δ_m^0, and δ_m^f is the displacement at failure. The nature of the stress (tensile or shear) determines each of the aforementioned quantities.

A damage variable value of zero indicates that the material remains in the elastic regime, whereas a value of one signifies complete failure of the cohesive element. In the cohesive element approach, an independent damage parameter D is allocated to every integration point. Consequently, each integration point within the element retains its own load-bearing capacity. The cohesive element is visually eliminated once the load-carrying capacity at all integration points reaches zero. The mechanical properties used in CZM for the adhesives are provided in Table 1.

2.2.2. Shear Damage Model

Although the criterion is predominantly employed in fracture modeling for ductile metals, its predictive accuracy can be effectively evaluated in homogeneous non-metallic materials, such as structural adhesives. The shear damage model predicts the onset of damage resulting from the accumulation of shear bands.

In this framework, the equivalent plastic strain at the onset of shear damage, $\bar{\varepsilon}_s^{pl}$, is postulated to be a function of the shear stress ratio θ_s and the equivalent plastic strain rate $\dot{\bar{\varepsilon}}^{pl}$; where $\theta_s = ((q + k_s P))/\tau_{max}$ denotes the shear stress ratio, q is von Mises equivalent stress, P is hydrostatic pressure, τ_{max} is the maximum shear stress, and k_s is a material-dependent parameter. Damage initiation occurs when the following scalar damage parameter ω_s reaches unity as indicated in Eq. (5) [39]:

$$\omega_s = \int \frac{\mathrm{d}\bar{\varepsilon}^{\mathrm{pl}}}{\bar{\varepsilon}_{\mathrm{s}}^{\mathrm{pl}}(\theta_{\mathrm{s}}.\,\dot{\bar{\varepsilon}}^{\mathrm{pl}})} = 1 \tag{5}$$

Upon damage initiation (ω_s), a linear softening law was adopted for the damage variable D ($0 \leq D \leq 1$). It degrades according to Eq. (6):

$$\sigma = (1 - D)\bar{\sigma} \tag{6}$$

where σ is the stress in the damaged state and $\bar{\sigma}$ is the stress in the undamaged state. The evolution of D is based on the fracture energy dissipation G_{II} (Eq. (7)) [33]:

$$D = \left(\frac{\bar{\varepsilon}^{pl} - \bar{\varepsilon}_s^{pl}}{\bar{\varepsilon}_f^{pl} - \bar{\varepsilon}_s^{pl}}\right) \qquad \bar{\varepsilon}_f^{pl} = \frac{2G_{II}}{\sigma_{eff} L_e} \tag{7}$$

where G_{II} is the Mode II fracture energy, L_e is the characteristic element length, and σ_{eff} is the effective stress at damage initiation.

The effective stress at damage initiation, σ_{eff}, is defined as the von Mises equivalent stress q evaluated at the instant when the shear damage parameter reaches unity ($\omega_s = 1$). Element deletion was enabled at $D = 1$ [36]. Equations (5) to (7) pertain to the concepts of the Shear Damage model in Abaqus software. The parameters entered into the software for the simulation include yield stress, fracture strain, fracture energy, and plastic strain (provided in Table 1). Furthermore, an isotropic hardening rule was employed for the plasticity relationships.

2.2.3. Simulation details

The simulation was conducted in a two-dimensional (2D) plane strain. In Abaqus, the single-lap adhesive joint was modeled as a single part, utilizing shell elements. This single part eliminates the need to define contact constraints between the adherends and the adhesive. Material properties, as detailed in previous sections, were assigned to the adhesive layer (Table 1) to predict the joint's tensile force using both the cohesive zone model (CZM) and the shear damage model. For joints with uniform adhesive, a single section was assigned to the adhesive. For graded adhesive (GA) configurations, multiple sections were defined (as illustrated in Fig. 1). The adherends are homogeneous elastic-plastic materials.

The simulation employed geometric nonlinearity (NLGEOM = YES). To apply boundary conditions, reference points were introduced at the ends of the adherends and kinematically coupled to the corresponding edges via coupling constraints. One end of the joint was fixed, whereas the opposing end was subjected to imposed displacement. In the field output request, SDEG was selected as the damage variable for the CZM, while DMICRT was designated as the damage initiation variable for the shear damage model. The STATUS field was activated to enable element deletion upon complete degradation. Plane-strain reduced-integration elements (CPE4R) were assigned to the adherends, and 2D cohesive elements (COH2D4) were used for the adhesive in the CZM approach. In contrast, CPE4R elements were employed for both adherends and adhesive in the shear damage model. It is well established that the CZM is mesh-insensitive with respect to element size [40]. Nonetheless, a mesh sensitivity analysis was performed, revealing that the cohesive element had a negligible influence on the joint failure load.

Consequently, the mesh was refined only to the extent necessary to minimize computational time, resulting in a global element size of 0.2 × 0.2 mm. For the shear damage model, results showed mesh dependency; thus, a convergence study was conducted. An adhesive zone element size of 0.05 mm was determined to yield converged results, as reported in the subsequent chapter.

2.3. Experiment design

The design of experiments (DOE) provides a cost-efficient approach that minimizes the total number of trials while effectively accounting for parameter interactions. In this research, to investigate the effect of adhesive gradation, the total adhesive thickness was fixed at 1.5 mm, with each adhesive layer having an equal thickness of 0.5 mm (three layers in total). The adherends were specified as aluminum and glass/epoxy composite. To study the effects of total adhesive thickness, adhesive layer thickness, and adherend type, response surface methodology (RSM) was employed using a central composite design (CCD) with α = 1.414 (rotatable), and one center point was adopted, resulting in a total of 27 runs.

Factor A (total adhesive thickness) was varied at five levels: 0.29, 0.5, 1.0, 1.5, and 1.7 mm. It was assumed that the thicknesses of the first and third layers are equal and represent a ratio of the middle (second) layer thickness. Accordingly, Factor B (adhesive layer thickness ratio), defined as the ratio of the outer layer thickness to the middle layer thickness, was incorporated at five levels: 0.29, 0.5, 1.0, 1.5, and 1.7.

Figure 6 illustrates the geometric variations corresponding to different levels of Factor B as an example. Factor C (adherend type) was treated as a categorical factor at three levels: Aluminum–Aluminum (Al–Al), Aluminum–Glass/epoxy (Al–GL), and Glass/epoxy–Glass/epoxy (GL–GL). Minitab 2021 software was used to design and analyze the simulations. According to the DOE, 27 test runs are required to simulate the tensile force.

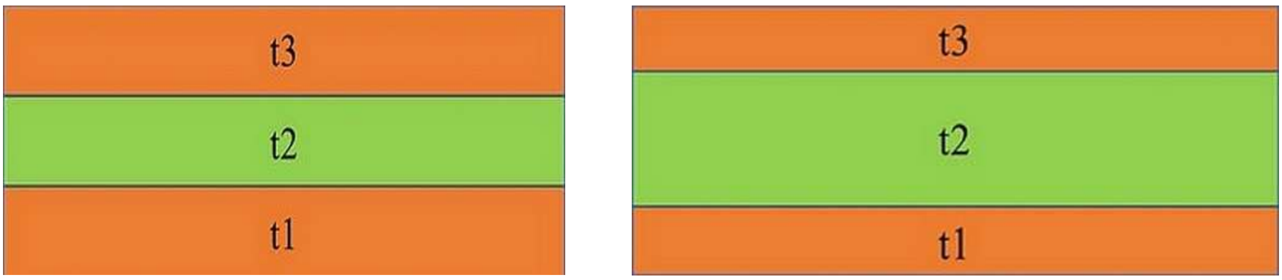

$t1 = t3 = \mathrm{B} \times t2, \mathrm{B} = 1$ $\qquad$ $\mathrm{t1} = \mathrm{t3} = \mathrm{B} \times \mathrm{t2}, \mathrm{B} = 0.5$

Fig. 6. Example of layer thickness ratio (Factor B).

3. Results and Discussion

3.1. Simulation verification

3.1.1. *Mesh study*

As detailed in Section 2.3.3, the shear damage model is sensitive to mesh refinement. Accordingly, an AL-AL single-lap joint incorporating the AV138 adhesive with a bondline thickness of 0.2 mm was modeled. Mesh convergence was assessed by progressively increasing the number of elements through the adhesive thickness from 1 to 5, while monitoring the predicted tensile force. The difference in tensile force between 4 and 5 elements was less than 1%, confirming adequate convergence. To balance numerical accuracy and computational cost, a mesh with four elements across the adhesive thickness corresponding to an element size of 0.05 mm was selected. Figure 7 shows the mesh sensitivity analysis (shear-damage approach).

3.1.2. *Comparison between the CZM and the Shear Damage Model*

As a benchmark case, the AL-AL single-lap joint with AV138 adhesive and a bondline thickness of 0.2 mm was simulated using both the CZM and the Shear Damage Model. The results were subsequently compared with those reported in the baseline article [29], as shown in Fig. 8. The CZM and Shear Damage Model predictions from the present study exhibit coefficients of correlation of R^2= 0.9 and R^2 = 0.97, respectively, relative to the experimental data from the reference. These values indicate excellent agreement between the two modeling approaches in predicting the joint's tensile force. This agreement is particularly good over the length L = 25, where all simulations related to the graded adhesive bond are performed at that length.

3.2. Graded adhesive (GA)

Following validation of the Shear Damage Model, it was employed to investigate the effect of adhesive grading along the bondline thickness. Initially, an AL-GL single-lap joint with AV138 adhesive and a uniform bondline thickness of 1.5 mm was simulated. Subsequently, a three-layer graded adhesive configuration, as defined in Section 2.2, was modeled in the thickness direction. The tensile load-carrying capacity was determined for both joint configurations. Both adhesive joints were fabricated in accordance with Figures 3-5 and subjected to experimental tensile loading. The force–displacement responses obtained from experimental tests are presented in Fig. 9. In Fig. 10, a comparison of the load-displacement results for the mono-adhesive and the graded-adhesive joints is presented.

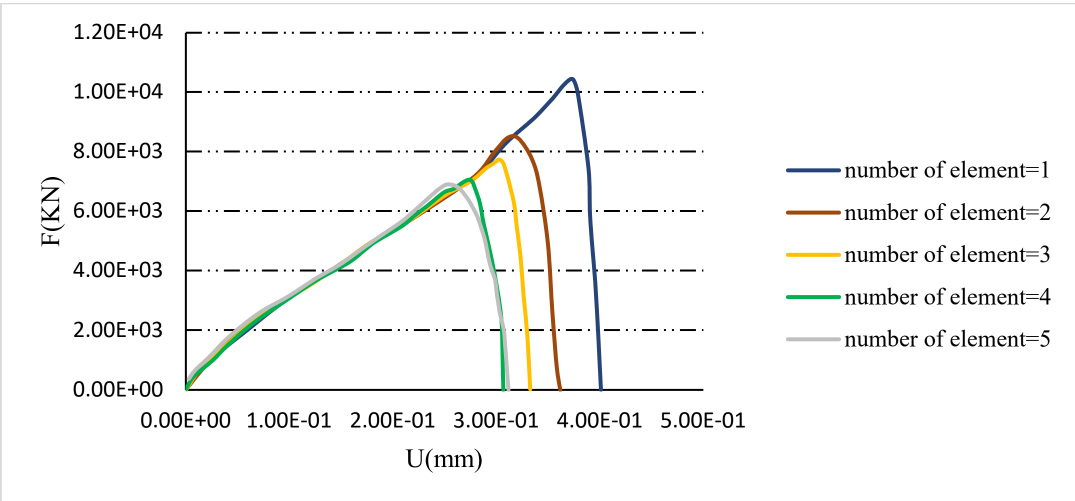

Fig. 7. Mesh study in shear damage model.

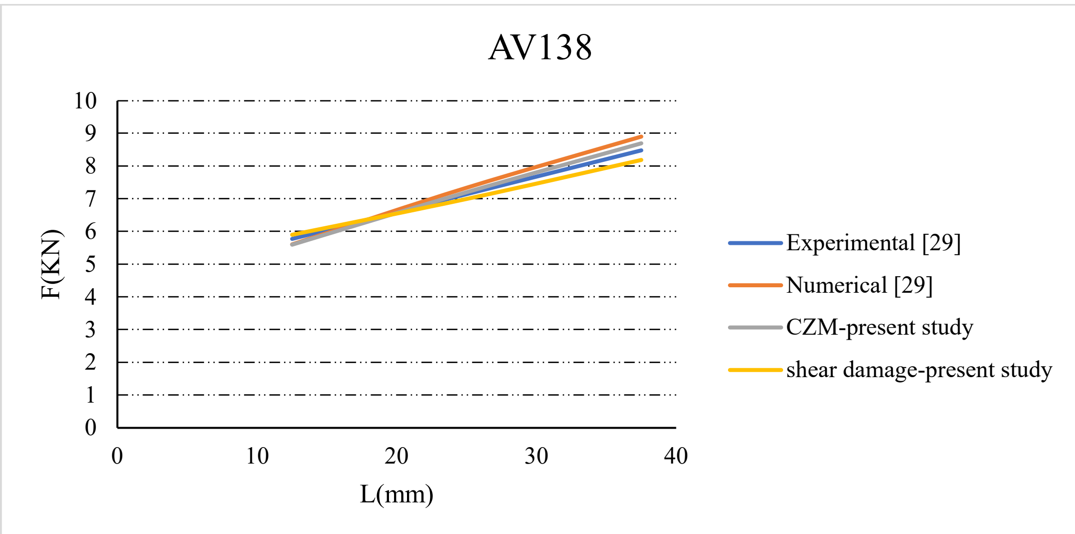

Fig. 8. Validation of CZM and shear damage.

In the mono AV138 adhesive joint, the brittle nature of the AV138 epoxy results in a linear increase in load up to the maximum tensile force, followed by a sudden failure and abrupt load drop. This behavior is attributed to stress concentrations at the overlap edges, leading to damage initiation and rapid crack propagation along the bondline. The numerical simulation demonstrates excellent agreement with the experimental results, with a peak load error of 7%.

In contrast, the graded adhesive joint exhibits a significant enhancement in toughness, with the peak load increasing by 48%. Moreover, no sudden load drop is observed post-peak, owing to the ductile SikaForce 7720 outer layers, which redistribute normal and shear stresses, thereby delaying damage initiation at the adhesive–adherent interfaces. The numerical results show a peak load error of 6.3%, indicating adequate predictive accuracy compared to the experimental data.

3.3. Stress distribution and damage contour

Figures 11 and 12 show the interfacial normal and shear stress distributions, respectively, at the adhesive interface of the AL-GL single-lap joint. As illustrated in Fig. 11, due to the bending moment induced by eccentric loading in the single-lap configuration, the maximum normal (peel) stress occurs at the ends of the overlap region. With the thickness-graded adhesive joint, the soft adhesive layer with a lower elastic modulus, which is in direct contact with the adherend, undergoes greater deformation and displacement. This results in a significant reduction in the interfacial normal stress. Moreover, the normal stress distribution becomes more uniform along the entire bondline. Reduction in peel stress reduces delamination and consequently enhances overall joint strength.

As shown in Fig. 12, softening the outer adhesive layer increases the shear strain absorption capacity. This leads to a reduction in interfacial shear stress. Additionally, the shear stress distribution becomes more uniform across the overlap region, which further contributes to the improvement of joint strength. Figure 13(a, b) show the contour of shear and normal stress distributions within the optimized adhesive joint. Due to the adherent configuration, the stress field is symmetrical. As depicted in Fig. 13, stress concentrations are most pronounced at the adhesive layer's overlapping edges, thereby initiating damage at these locations.

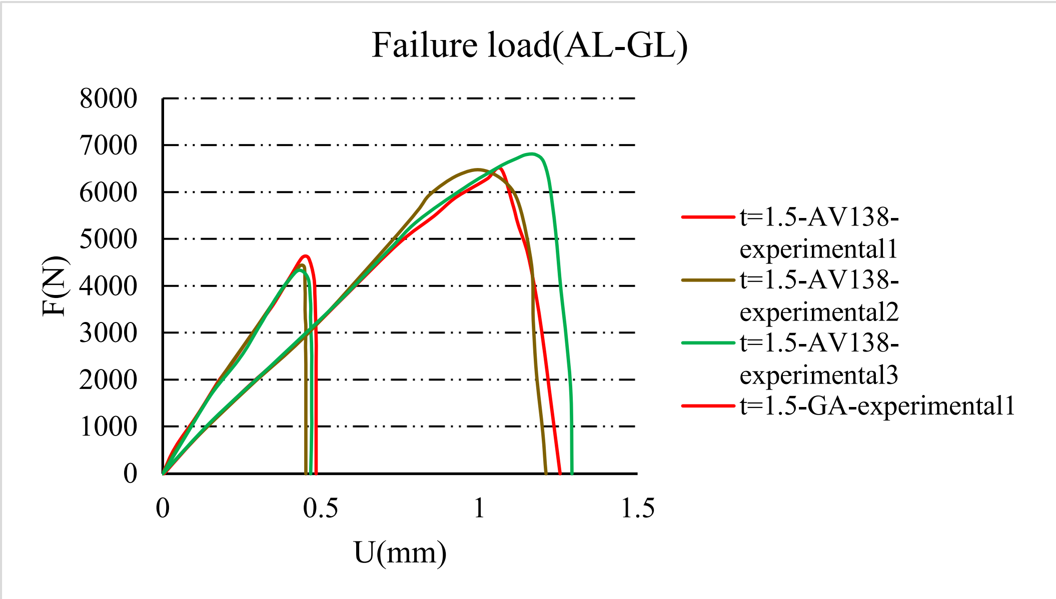

Fig. 9. Experimental force-displacement plot of adhesive joints.

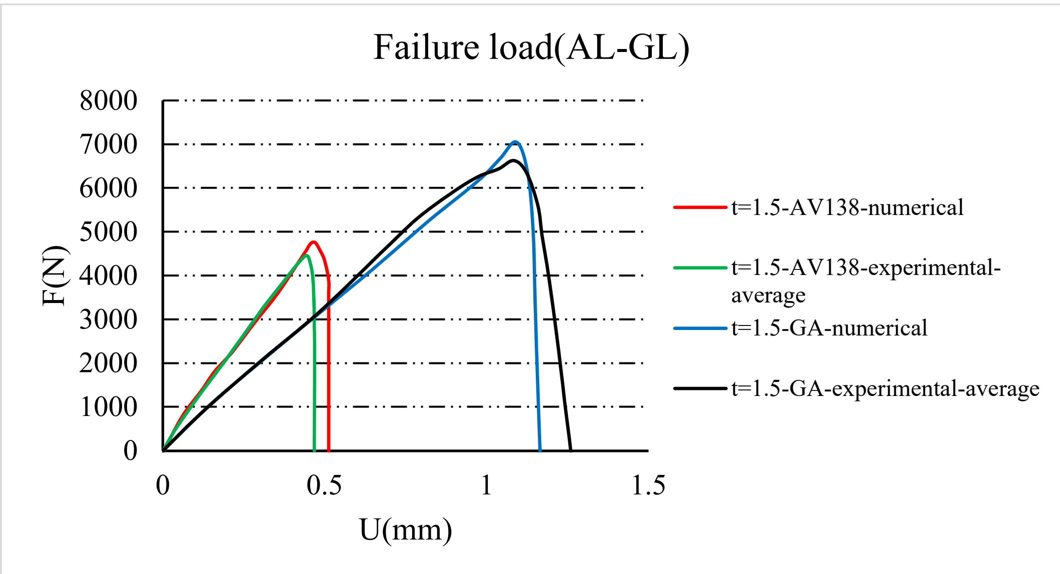

Fig. 10. Comparison of numerical and experimental force-displacement mono-adhesive and graded-adhesive joint plots.

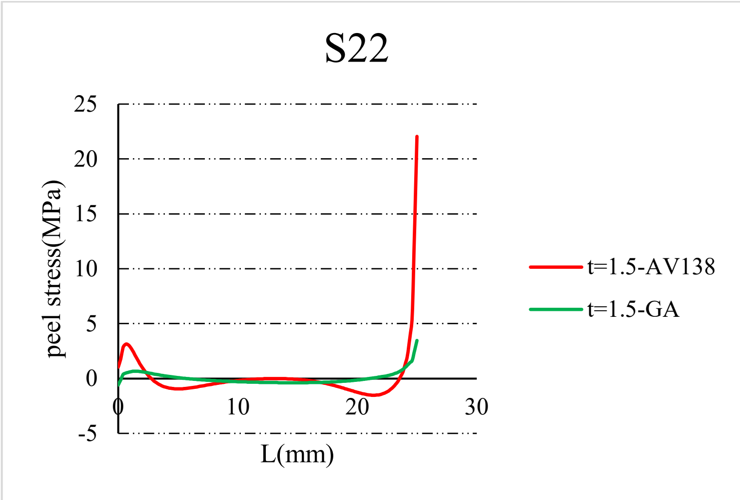

Fig. 11. Interfacial normal (peel) stress distribution in AL-GL.

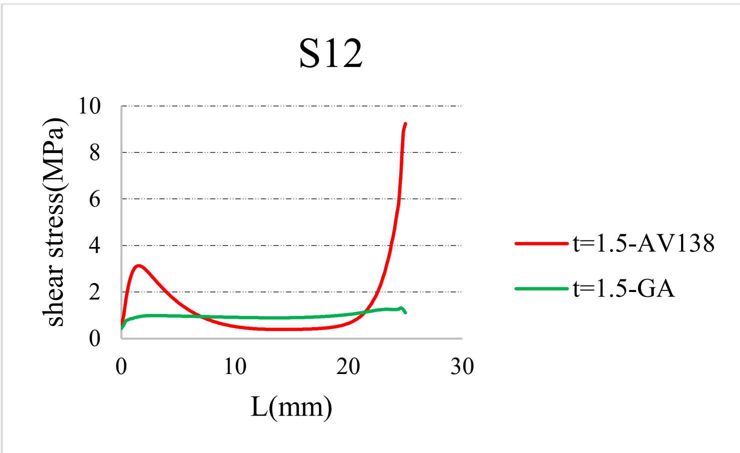

Fig. 12. Interfacial shear stress distribution in AL-GL.

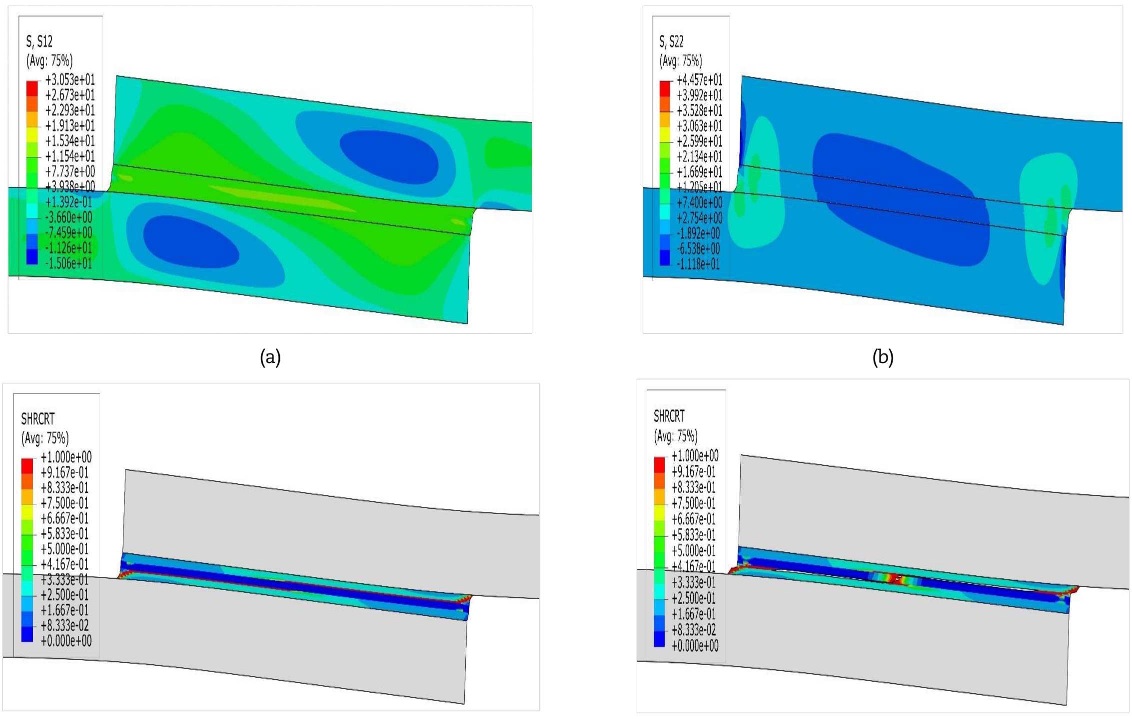

Fig. 13. (a) Shear stress; (b) Normal stress; (c) Damage initiation; (d) Damage propagation and failure of adhesive.

Table 2. Tensile force results of the adhesive joint based on DOE.

Run	A	B	C	Force (N) (Simulation)	Force (N) (Prediction of regression equation)	Error (%)
1	0.5	0.5	AL-AL	6870.73	6885.54	0.21
2	1.5	0.5	AL-AL	6940.2	6942.16	0.03
3	0.5	1.5	AL-AL	6935.88	6972.05	0.52
4	1.5	1.5	AL-AL	7055.4	7028.68	0.37
5	0.5	1.0	AL-AL	6917.91	6920.34	0.03
6	1.5	1.0	AL-AL	7026.46	7000.42	0.37
7	1.0	0.5	AL-AL	6884.38	6892.65	0.12
8	1.0	1.5	AL-AL	7001.71	7015.01	0.18
9	1.0	1.0	AL-AL	7172.64	7147.83	0.34
10	0.5	0.5	AL-GL	7083.51	7082.73	0.01
11	1.5	0.5	AL-GL	7164.93	7139.36	0.35
12	0.5	1.5	AL-GL	6890.4	6808.05	1.1
13	1.5	1.5	AL-GL	6802.31	6864.68	0.91
14	0.5	1.0	AL-GL	6870.2	6936.94	0.97
15	1.5	1.0	AL-GL	6957.3	7017.02	0.86
16	1.0	0.5	AL-GL	7200.1	7164.66	0.49
17	1.0	1.5	AL-GL	6816.34	6776.20	0.58
18	1.0	1.0	AL-GL	7170.43	7164.43	0.07
19	0.5	0.5	GL-GL	7196.85	7099.98	1.3
20	1.5	0.5	GL-GL	7200.32	7156.60	0.60
21	0.5	1.5	GL-GL	7010.30	6982.68	0.39
22	1.5	1.5	GL-GL	7080.12	7039.30	0.57
23	0.5	1.0	GL-GL	7015.35	7032.87	0.24
24	1.5	1.0	GL-GL	7120.24	7112.95	0.09
25	1.0	0.5	GL-GL	7040.54	7149.31	1.55
26	1.0	1.5	GL-GL	6925.31	6983.42	0.84
27	1.0	1.0	GL-GL	7230.42	7260.37	0.42

Table 3. Variance analysis for tensile force.

Source	DF	Adj SS	Adj MS	F-value	P-value
Model	8	376183	47023	15.02	0.000
Linear	4	147867	36967	11.81	0.000
A	1	19237	19237	6.15	0.023
B	1	62203	62203	19.88	0.000
C	2	66427	33213	10.61	0.001
Square	2	97133	48567	15.52	0.000
A*A	1	76666	76666	24.50	0.000
B*B	1	82116	82116	26.24	0.000
2-Way Interaction	2	131183	65591	20.96	0.000
B*C	2	131183	65591	20.96	0.000
Error	18	56334	3130		
Total	26	432517			
R_0^2 = 87%		R_A^2 = 81%		R_P^2 = 69%	

Figures 13(c, d) present the evolution of the damage initiation parameter SHRCRT across progressive stages, from damage onset through propagation to final adhesive failure. As shown in Fig. 13(c), consistent with the elevated stress levels, damage (indicated by the red region where SHRCRT = 1) originates at the overlap edges. In Fig. 13(d), the damage front propagates toward the mid-region of the adhesive and the interface between the two adhesive layers. Ultimately, complete failure occurs in the central adhesive layer.

3.4. Variance analysis

As detailed in section 2.4, the 27 run configurations generated via VOE were numerically simulated under varying parametric conditions and subjected to uniaxial tensile loading. Additionally, the maximum tensile load sustained by the adhesive joint was recorded for every run and is summarized in Table 2. Analysis of variance (ANOVA) was used to investigate the effects of total adhesive thickness, adhesive layer thickness, and adherend type on the joint's tensile force.

ANOVA was performed using a quadratic model to evaluate the main effects and interaction effects among the parameters. Table 3 shows the analysis of variance for tensile force. In the ANOVA, a P-value less than 0.05 indicates statistical significance of the variable. Additionally, a higher F-value indicates a stronger effect of the variable on the response. As in Table 3, total adhesive thickness, adhesive layer thickness, and adherend type are significant for the joint's tensile force. The F-values in Table 3 indicate that the nonlinear effects of the parameters are greater than the impact of linear effects. As depicted in Figure 14, Pareto charts and normal-probability plots were employed to identify significant and non-significant factors.

In the normal probability plot, parameters deviating substantially from the normal line are deemed statistically significant. Similarly, in the Pareto chart, factors exceeding the reference threshold are considered significant.

3.5. Main and interaction effects

As observed in Fig. 15, the main effects plots reveal non-linear behavior for the quantitative factors A (total adhesive thickness) and B (layer thickness ratio), and the categorical factor C (adherend type) shows an increasing trend from Al-Al to GL-GL.

Specifically, both A and B demonstrate that increasing thickness up to a critical value enhances joint strength. Increasing beyond that critical point reduces load-carrying capacity.

Da Silva and Quan [41, 42] reported nonlinear adhesive thickness-strength behavior in their study, characterized by an increase up to a critical thickness followed by a subsequent decline. They attributed this phenomenon to the extent of the plastic zone formed around the crack tip. Interaction plots indicate that the A×B and A×C lines are nearly parallel, signifying negligible interaction between these parameter pairs. In contrast, the B×C plot shows non-parallel lines with crossovers, confirming significant interactions between B and C. As illustrated in the A×B graph, increasing the ductile-to-brittle adhesive thickness enhances joint strength, reaching a maximum at an optimal ratio.

This enhancement is more pronounced at a total adhesive thickness of 1.0 mm compared to 0.5 mm or 1.5 mm. The A×C graph confirms that GL–GL joints yield the highest strength. The B×C interaction graph further reveals that increasing the total adhesive thickness from 0.5 mm to 1.5 mm increases strength in Al-AL joints but reduces it in GL-GL and Al-GL configurations.

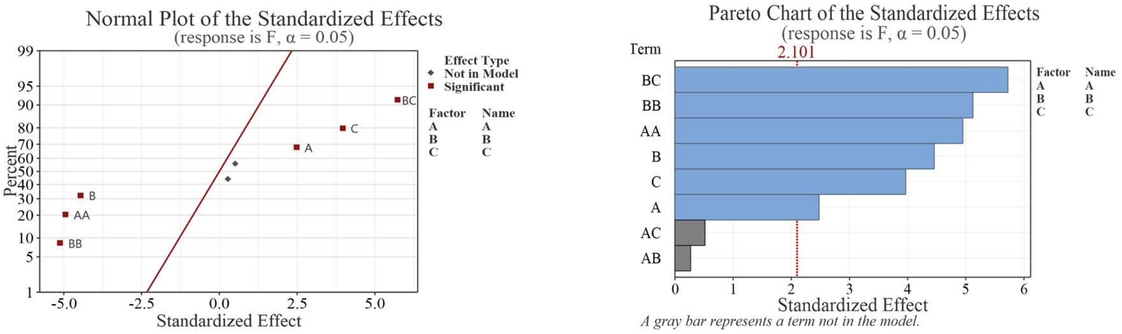

(a) (b)

Fig. 14. Significant effects: (a) Normal plot, (b) Pareto plot.

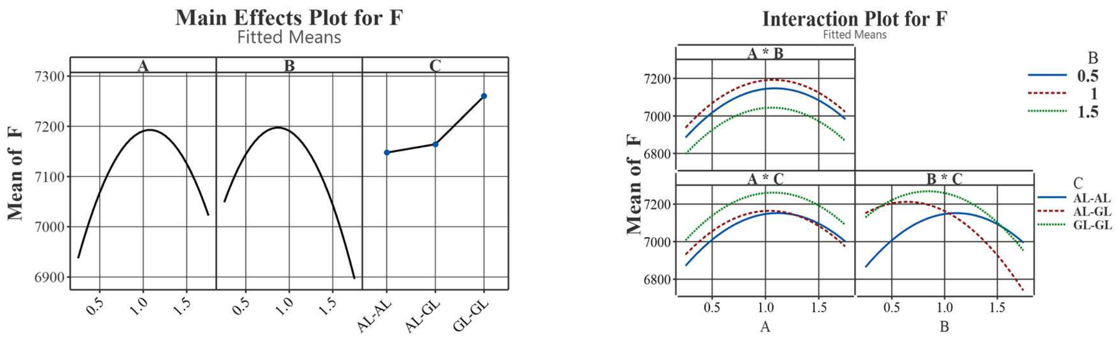

(a) (b)

Fig. 15. (a) Main, (b) Interaction effects plot.

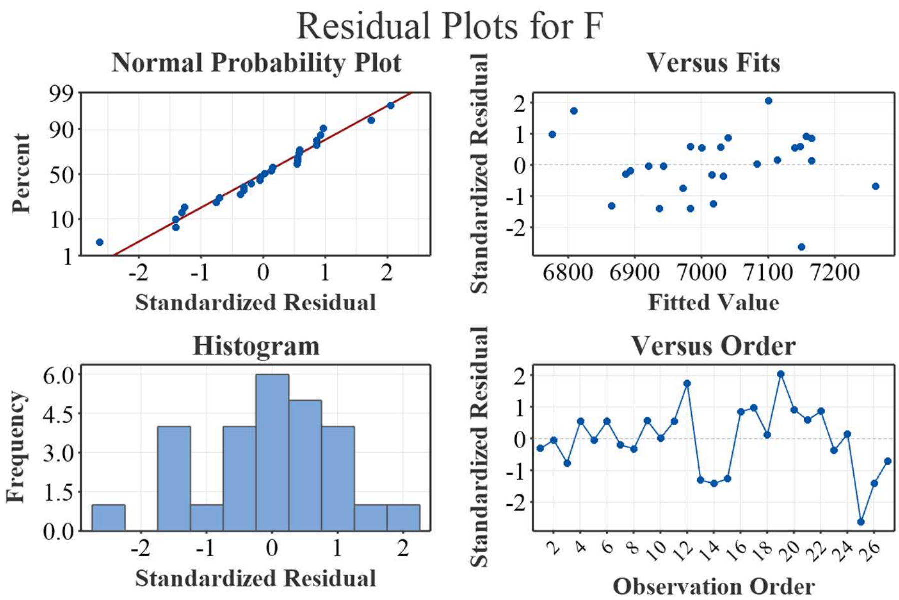

Fig. 16. Statistical plots for model adequacy.

Table 4. The results of the optimization and validation at the parameters' optimal values.

Responses	Experimental	Numerical	Prediction of regression
Tensile force (N)	6806	7248	7271
		Error = 6.5%	Error = 6.8%

3.6. Adequacy of the model

In Fig. 16, the model's adequacy diagnostics are presented. In Fig. 16(a), (Normal probability plot of residuals), data points align closely with the crimson line, confirming normality. In Fig. 16(b), (Histogram of residuals), symmetric distributions are centered around zero, further validating normality. In Fig. 16(c), (Residuals vs. predicted values), there is no systematic pattern indicating homoscedasticity and model appropriateness. In Fig. 16(d), (Residuals vs. run order), the random scatter confirms the independence of the residuals. These diagnostic checks collectively affirm the statistical validity and predictive reliability of the developed response surface model.

3.7. Regression equation

To evaluate the predictive capability of the ANOVA model for tensile force, the variables R_0^2, R_A^2, and R_P^2 were used, as indicated in Table 3. The superior predictive accuracy of the analysis of variance (ANOVA) model was evidenced by higher values of R_0^2, R_A^2, and R_P^2. It is evident from Table 3 that the value of R_0^2 is close to 87%, validating the prediction ability of the estimated variance analysis model for the tensile force.

Regression was employed to quantify the effects of the investigated parameters on the research outcomes; specifically, quadratic regression to model response variation. In this study, the regression equation predicted the tensile force within a 95% confidence interval (CI), with statistical significance of $p < 0.05$. Regression modeling elucidated the relationship between the input parameters and the resulting response. Accordingly, a quadratic regression model was developed to predict adhesive tensile force using the selected parameters (the following equation).

The regression equation was computed separately for each adherent joint:

$$\text{AL-AL:} \quad F = 6242 + 806\,A + 863\,B - 374.9\,A^2 - 388.0\,B^2 \tag{8}$$

$$\text{AL-GL:} \quad F = 6620 + 806\,A + 501\,B - 374.9\,A^2 - 388.0\,B^2 \tag{9}$$

$$\text{GL-GL:} \quad F = 6558 + 806\,A + 659\,B - 374.9\,A^2 - 388.0\,B^2 \tag{10}$$

As presented in Table 3, the tensile load of the adhesive joint was predicted using the regression equations for various factor levels. These predicted values exhibit minimal deviation from the numerical simulation results, which can be attributed to the strong agreement between the regression model and the finite element analysis.

3.8. Optimization by desirability function

To identify the optimal parameter settings for maximizing the tensile force of the adhesive joint, the desirability function approach was implemented [36]. The ANOVA results were incorporated into the desirability function procedure to determine the optimum parameter combination. Specifically, the predictive model derived from ANOVA was converted into a desirability index (d). This index ranges from 0 to 1, where $d = 0$ signifies that the predicted response is substantially outside the target range, and $d = 1$ indicates a fully desirable outcome. The desirability function is formulated based on three optimization objectives: (i) maximization of the response, (ii) minimization of the response, and (iii) targeting a specific response value. In the present study, the objective was to maximize the tensile force of the adhesive joint; accordingly, the maximization goal was selected. The corresponding desirability function for maximizing the response is expressed as follows:

$$\begin{cases} 0 & y < L \\ \left(\dfrac{y-L}{G-L}\right)^n & L \le y \le G \\ 1 & y > G \end{cases} \tag{11}$$

In this formulation, L and G represent the lower bound and target value of the response, respectively, while n denotes the response weight, typically set to unity. The desirability function was computed using Minitab 2021 software. Desirability analysis yielded the optimal solution with a composite desirability of $D = 1.0$, corresponding to a total adhesive thickness of 1.07 mm, a layer thickness ratio of 0.85, and a GL-GL adherend combination. At this optimum, the predicted ultimate tensile load of the joint was 7271 N.

3.9. Verification test

To verify the optimization results, a numerical simulation and experimental tests of the adhesive joint were conducted using the identified optimal parameter values. The maximum tensile force under this optimal configuration was then extracted for comparison with the predictions from the desirability function approach. Table 4 provides a comparative summary of the optimization, simulation, and experimental results at the optimal condition. As demonstrated in Table 4, the validation results exhibit strong agreement with the values predicted by the desirability function procedure.

4. Conclusions

This study investigated the effect of adhesive grading along the bondline thickness. Joint specimens were fabricated experimentally and subjected to mechanical testing. Numerical simulations were conducted to predict joint strength. RSM was employed to analyze design effects and optimize performance. The obtained results are listed below:

- The results revealed that the shear damage model accurately simulates adhesive behavior in the software, exhibiting strong agreement with the cohesive zone model (CZM) and a maximum error of less than 7% relative to the experimental data.

- Grading the adhesive along the bondline thickness and positioning the ductile adhesive in contact with the adherents alters the stress distribution, thereby enhancing the joint strength. The graded adhesive joint had a 48% increase in strength and enhanced toughness compared to the mono-brittle adhesive joint.
- The through-thickness graded adhesive configuration significantly increases the area under the load–displacement curve, which corresponds to a notable improvement in the fracture toughness and energy absorption capacity of the joint. This enhanced toughness is particularly beneficial under dynamic loading conditions (for example, fatigue and impact), where greater energy dissipation capacity is required.
- ANOVA revealed that total adhesive thickness, thickness ratio of adhesive layers, and adherend type significantly influence joint strength. A quadratic regression model was developed to predict the tensile load, where nonlinear effects predominated over linear effects. The proposed model exhibits excellent agreement with the numerical simulation results.
- Joint strength increased progressively from AL-AL to GL-AL, and further to GL-GL adherend combinations. Furthermore, a significant interaction exists between adherend type and adhesive layer thickness ratio.
- It was estimated that the maximum tensile force could be achieved with a total adhesive thickness of 1 mm, a layer thickness ratio of 0.85, and an adherent type of GL-GL. It was also predicted that with optimized parameters, the adhesive's tensile force would reach 7271 N.
- The verification test results under the optimal condition exhibited strong agreement with the desirability function predictions. Additionally, contour plots of stress distribution and stiffness degradation in the adhesive layer confirmed robust joint strength at the optimized parameter settings

Author Contributions

S.M.M.M.H. Ahari conducted the experiments, analyzed the results, developed the numerical modeling and examined the validation. The manuscript was written through the contribution of all authors. All authors planned the scheme, initiated the project and suggested the experiments; discussed the results, reviewed and approved the final version of the manuscript.

Acknowledgments

Not applicable.

Conflict of Interest

The authors declared no potential conflicts of interest concerning the research, authorship, and publication of this article.

Funding

The authors received no financial support for the research, authorship, and publication of this article.

Data Availability Statements

The datasets generated and/or analyzed during the current study are available from the corresponding author on reasonable request.

References

[1] Gavgali, E., Sahin, R., Akpinar, S., An investigation of the fatigue performance of adhesively bonded STEP-lap joints: An experimental and numerical analysis, *International Journal of Adhesion and Adhesives*, 104, 2021, 102736.
[2] Jia, Z., Yuan, G., Feng, X., Zou, Y., Yu, J., Shear properties of polyurethane ductile adhesive at low temperatures under high strain rate conditions, *Composites Part B: Engineering*, 156, 2019, 292–302.
[3] Marques, J., Barbosa, A., Da Silva, C., Carbas, R., Da Silva, L., An overview of manufacturing functionally graded adhesives–Challenges and prospects, *The Journal of Adhesion*, 97(2), 2021, 172–206.
[4] Amidi, S., Wang, J., Three-parameter viscoelastic foundation model of adhesively bonded single-lap joints with functionally graded adherends, *Engineering Structures*, 170, 2018, 118–134.
[5] Khan, M., Tipireddy, R., Dattaguru, B., Kumar, S., Stochastic modeling of functionally graded double lap adhesive joints, *Mechanics of Materials*, 177, 2023, 104553.
[6] Kumar, D., Budarapu, P., Pradhan, A., Numerical analysis of lap shear joints made of functionally graded materials, *Journal of the Brazilian Society of Mechanical Sciences and Engineering*, 45(2), 2023, 94.
[7] Dorduncu, M., Apalak, M. K., Reddy, J., Stress wave propagation in a through-thickness functionally graded adhesive layer, *Journal of Adhesion Science and Technology*, 33(21), 2019, 2329–2355.
[8] Durodola, J., Functionally graded adhesive joints–A review and prospects, *International Journal of Adhesion and Adhesives*, 76, 2017, 83–89.
[9] Nimje, S., Panigrahi, S., Design and analysis of functionally graded adhesively bonded double supported tee joint of laminated FRP composite plates under varied loading, *Journal of Adhesion Science and Technology*, 29(18), 2015, 1951–1970.
[10] Gustafson, P. A., Bizard, A., Waas, A. M., Dimensionless parameters in symmetric double lap joints: An orthotropic solution for thermomechanical loading, *International Journal of Solids and Structures*, 44(17), 2007, 5774–5795.
[11] Dadian, A., Rahnama, S., Experimental and numerical study of optimum functionally graded Aluminum/GFRP adhesive lap shear joints using Epoxy/CTBN, *International Journal of Adhesion and Adhesives*, 107, 2021, 102854.
[12] Kim, M.-H., Hong, H.-S., Kim, Y.-C., Determination of failure envelope of functionally graded adhesive bonded joints by using mixed mode continuum damage model and response surface method, *International Journal of Adhesion and Adhesives*, 106, 2021, 102815.
[13] Breto, R., Chiminelli, A., Duvivier, E., Lizaranzu, M., Jimenez, M., Functionally graded bond-lines for metal/composite joints, *European Conference on Composite Materials*, Seville, Spain, 2014.
[14] Jia, Z., Yu, J., Liu, Q., Yu, S., Wang, Z., Functionally graded adhesive joints with exceptional strength and toughness by graphene nanoplatelets reinforced epoxy adhesives, *International Journal of Adhesion and Adhesives*, 125, 2023, 103402.
[15] Adams, R., Peppiatt, N., Stress analysis of adhesive-bonded lap joints, *Journal of Strain Analysis*, 9(3), 1974, 185–196.
[16] Crocombe, A., Global yielding as a failure criterion for bonded joints, *International Journal of Adhesion and Adhesives*, 9(3), 1989, 145–153.
[17] Gleich, D., Van Tooren, M., Beukers, A., Analysis and evaluation of bondline thickness effects on failure load in adhesively bonded structures, *Journal of Adhesion Science and Technology*, 15(9), 2001, 1091–1101.
[18] Grant, L., Adams, R. D., Da Silva, L. F., Experimental and numerical analysis of single-lap joints for the automotive industry, *International Journal of Adhesion and Adhesives*, 29(4), 2009, 405–413.
[19] Ciardiello, R., Boursier Niutta, C., Goglio, L., Adhesive thickness and ageing effects on the mechanical behaviour of similar and dissimilar single

lap joints used in the automotive industry, *Processes*, 11(2), 2023, 433.
[20] Wang, Z., Li, C., Sui, L., Xian, G., Effects of adhesive property and thickness on the bond performance between carbon fiber reinforced polymer laminate and steel, *Thin-Walled Structures*, 158, 2021, 107176.
[21] Saleh, M. N., Budzik, M. K., Saeedifar, M., Zarouchas, D., De Freitas, S. T., On the influence of the adhesive and the adherend ductility on mode I fracture characterization of thick adhesively-bonded joints, *International Journal of Adhesion and Adhesives*, 115, 2022, 103123.
[22] Metehri, A., Madani, K., Campilho, R. D., Numerical analysis of the geometrical modifications effects on the tensile strength of bonded single-lap joints, *International Journal of Adhesion and Adhesives*, 134, 2024, 103814.
[23] Rangaswamy, H., Sogalad, I., Basavarajappa, S., Acharya, S., Manjunath Patel, G., Experimental analysis and prediction of strength of adhesive-bonded single-lap composite joints: Taguchi and artificial neural network approaches, *SN Applied Sciences*, 2(6), 2020, 1055.
[24] Morgado, M., Carbas, R., Dos Santos, D., Da Silva, L., Strength of CFRP joints reinforced with adhesive layers, *International Journal of Adhesion and Adhesives*, 97, 2020, 102475.
[25] Dos Santos, D., Carbas, R., Marques, E., Da Silva, L., Reinforcement of CFRP joints with fibre metal laminates and additional adhesive layers, *Composites Part B: Engineering*, 165, 2019, 386–396.
[26] Sugiman, S., Ahmad, H., Comparison of cohesive zone and continuum damage approach in predicting the static failure of adhesively bonded single lap joints, *Journal of Adhesion Science and Technology*, 31(5), 2017, 552–570.
[27] Özer, H., Öz, Ö., The use of the exponential Drucker-Prager material model for defining the failure loads of the mono and bi-adhesive joints, *International Journal of Adhesion and Adhesives*, 76, 2017, 17–29.
[28] Kumar, S., Pandey, P., Behaviour of bi-adhesive joints, *Journal of Adhesion Science and Technology*, 24(7), 2010, 1251–1281.
[29] Rocha, R., Campilho, R., Evaluation of different modelling conditions in the cohesive zone analysis of single-lap bonded joints, *The Journal of Adhesion*, 94(7), 2018, 562–582.
[30] Simon Portillo, F. J., Cuadrado Sempere, O., Marques, E., Sanchez Lozano, M., Da Silva, L. F. M., Mechanical characterization and comparison of hyperelastic adhesives: Modelling and experimental validation, *Journal of Applied and Computational Mechanics*, 8(1), 2022, 359–369.
[31] Shishesaz, M., Ghamarian, A. H., Mosalmani, R., The effects of defects and adherend material on adhesive stress distribution in laminated composite tubular joints under axial tensile loads, *Journal of Applied and Computational Mechanics*, 11(4), 2025, 1112–1138.
[32] He, Z., Zheng, G., Luo, Q., Li, Q., Sun, G., Fatigue damage tolerance of CFRP/Al adhesive joints with thermal effects, *International Journal of Mechanical Sciences*, 281, 2024, 109543.
[33] Wei, Y., Zheng, G., Luo, Q., Li, Q., Sun, G., On impact response and damage tolerance of adhesively bonded joints–An experimental and numerical study, *Thin-Walled Structures*, 208, 2025, 112606.
[34] Kujawa, M., Smakosz, Ł., Paczos, P., Jan, F., Winkelmann, K., Konopinska-Zmysłowska, V., Eremeyev, V., An analytical, finite element and experimental study of single-lap joints bonded with epoxy adhesive, *International Journal of Engineering Science*, 226, 2026, 104555.
[35] Sika Industry, *Structural adhesives*, Sika Industry, accessed 2025, https://industry.sika.com/en/home/transportation/structural-adhesives.
[36] Samadi, M. R., Alaei, M. H., Eskandari Jam, J., Numerical investigation of the strength of Al/GFRP adhesive bonding under tensile loading, *Journal of Polymer Engineering*, 44(2), 2024, 145–154.
[37] MatWeb, *Materials Park, MatWeb*, accessed 2025, https://asm.matweb.com.
[38] ASTM International, *Standard test method for lap shear adhesion for fiber reinforced plastic (FRP) bonding*, ASTM International, 2014.
[39] *ABAQUS Documentation*, Dassault Systèmes, 2009.
[40] Feih, S., Shercliff, H., Adhesive and composite failure prediction of single-L joint structures under tensile loading, *International Journal of Adhesion and Adhesives*, 25(1), 2005, 47–59.
[41] Da Silva, L. F., Rodrigues, T., Figueiredo, M., De Moura, M., Chousal, J., Effect of adhesive type and thickness on the lap shear strength, *The Journal of Adhesion*, 82(11), 2006, 1091–1115.
[42] Quan, D., Murphy, N., Ivankovic, A., Fracture behaviour of a rubber nano-modified structural epoxy adhesive: Bond gap effects and fracture damage zone, *International Journal of Adhesion and Adhesives*, 77, 2017, 138–150.

ORCID iD

Author 1 https://orcid.org/0000-000x-xxxx-xxxx
Author 2 https://orcid.org/0000-000x-xxxx-xxxx
Author 3 https://orcid.org/0000-000x-xxxx-xxxx

How to cite this article: Ahari S.M.M.M.H. et al., Statistical, Numerical, and Experimental Analysis of Thickness-Graded Adhesive for Enhancing Single-Lap Joint Strength, *J. Appl. Comput. Mech.*, xx(x), 2026, 1–14.
https://doi.org/10.22055/jacm.2026.49138.5760